The Astrophysical Journal, 991:170 (10pp), 2025 October 1 https://doi.org/10.3847/1538-4357/ae019f

Tracing the Origins of Hot Halo Gas in Milky Way–type Galaxies with SMUGGLE

Zhijie Zhang (张志杰)[1], Xiaoxia Zhang (张小霞)[1], Hui Li (李辉)[2,3], Taotao Fang (方陶陶)[1], Yang Luo (罗阳)[4], Federico Marinacci[5,6], Laura V. Sales[7], Paul Torrey[8], Mark Vogelsberger[9], Qingzheng Yu (余清正)[10], and Feng Yuan (袁峰)[11]

[1] Department of Astronomy, Xiamen University, Xiamen, Fujian 361005, People's Republic of China; zhangxx@xmu.edu.cn, fangt@xmu.edu.cn
[2] Department of Astronomy, Tsinghua University, Beijing 100084, People's Republic of China; hliastro@tsinghua.edu.cn
[3] Department of Astronomy, Columbia University, Manhattan, NY 10027, USA
[4] Department of Astronomy, Yunnan University, Kunming, Yunnan 650000, People's Republic of China
[5] Department of Physics and Astronomy "Augusto Righi," University of Bologna, via Gobetti 93/2, I-40129 Bologna, Italy
[6] INAF, Astrophysics and Space Science Observatory Bologna, Via P. Gobetti 93/3, I-40129 Bologna, Italy
[7] Department of Physics and Astronomy, University of California, Riverside, 900 University Avenue, Riverside, CA 92521, USA
[8] Department of Astronomy, University of Virginia, 530 McCormick Road, Charlottesville, VA 22903, USA
[9] Department of Physics and Kavli Institute for Astrophysics and Space Research, Massachusetts Institute of Technology, Cambridge, MA 02139, USA
[10] Dipartimento di Fisica e Astronomia, Università degli Studi di Firenze, Via G. Sansone 1, 50019 Sesto Fiorentino, Firenze, Italy
[11] Center for Astronomy and Astrophysics and Department of Physics, Fudan University, Shanghai 200438, People's Republic of China
Received 2025 July 14; revised 2025 August 15; accepted 2025 August 29; published 2025 September 26

Abstract

Current galaxy formation models predict the existence of X-ray-emitting gaseous halos around Milky Way (MW)–type galaxies. To investigate properties of this coronal gas in MW-like galaxies, we analyze a suite of high-resolution simulations based on the SMUGGLE framework and compare the results with X-ray observations of both the MW and external galaxies. We find that for subgrid models incorporating any form of stellar feedback, e.g., early feedback (including stellar winds and radiation) and/or supernova (SN) explosions, the total 0.5–2 keV luminosity is consistent *within uncertainties* with X-ray observations of the MW and with scaling relations derived for external disk galaxies. However, all models exhibit an X-ray surface brightness profile that declines too steeply beyond ∼5 kpc, underpredicting the extended emission seen in recent eROSITA stacking results. Across all subgrid prescriptions, the simulated surface brightness and emission measure fall below MW observations by at least 1–2 orders of magnitude, with the most severe discrepancy occurring in the no-feedback model. Our results suggest that (i) stellar feedback primarily shapes the innermost hot atmosphere (central ∼5 kpc), with comparable contributions from early feedback and SNe to the resulting X-ray luminosity; (ii) additional mechanisms such as gravitational heating, active galactic nuclei feedback, and/or Compton effects of GeV cosmic ray are necessary to generate the extended, volume-filling hot gaseous halo of MW-mass galaxies; (iii) the origins of hot corona in MW-like galaxies are partially distinct from those of the warm ($\sim 10^5$ K) gas, by combining our previous finding that the SMUGGLE model successfully reproduces the kinematics and spatial distribution of MW O VI absorbers.

Unified Astronomy Thesaurus concepts: Hot ionized medium (752); Stellar feedback (1602); Interstellar medium (847); Circumgalactic medium (1879); Diffuse radiation (383)

1. Introduction

The presence of extended X-ray coronae around massive galaxies has long been predicted by galaxy formation theory (e.g., L. Spitzer 1956; S. D. M. White & M. J. Rees 1978; S. D. M. White & C. S. Frenk 1991). In the standard picture of galaxy formation, infalling gas from the intergalactic medium (IGM) experiences accretion shocks, heating it to the galaxy's virial temperature ($T \gtrsim 10^6$ K). For massive ($M_{\rm vir} \gtrsim 10^{12}\,M_\odot$) galaxies, the cooling time of the shock-heated gas is sufficiently long to establish a quasi-hydrostatic equilibrium, forming a volume-filling, X-ray-emitting gaseous halo (e.g., Y. Oren et al. 2024). Lower-mass galaxies, due to their shallower potential wells, are generally expected to host fainter X-ray coronae. The properties of their hot gas are expected to be shaped by feedback from stellar winds, supernovae (SNe; e.g., D. K. Strickland et al. 2004; R. A. Crain et al. 2010; R. Davé et al. 2012; A. Sokołowska et al. 2018), and active galactic nuclei (AGN; e.g., N. Truong et al. 2020). However, for Milky Way (MW) analogues ($M_{\rm vir} \sim 10^{12}\,M_\odot$), which lie at the boundary between these mass regimes, there is no consensus on the dominant heating mechanism.

Observationally, the hot gaseous halo of our Galaxy has been detected both in emission as a component of the soft X-ray background (e.g., D. B. Henley & R. L. Shelton 2013; Z. Pan et al. 2024) and in absorption (e.g., O VII and O VIII) in high-resolution X-ray spectra of background sources (e.g., T. Fang et al. 2003, 2006, 2015; Y. Luo et al. 2018). These observations yield a characteristic temperature of $T \approx 2 \times 10^6$ K, though this value remains model-dependent. With the high spatial resolution of Chandra, extraplanar X-ray emission has been detected for external, mostly edge-on disk galaxies, to minimize point-source contamination. Those observations targeted galactic central regions, revealing typical scale heights of 1–30 kpc, with a median value of ∼5 kpc (e.g., D. K. Strickland et al. 2004; R. Tüllmann et al. 2006; J.-T. Li & Q. D. Wang 2013a). Furthermore, tight correlations were revealed between X-ray luminosity ($L_{\rm X}$) and star formation

rate (SFR), indicating hot gas origins associated with stellar activity (e.g., J.-T. Li & Q. D. Wang 2013b; Q. D. Wang et al. 2016). However, the L_X–SFR relation may alternatively reflect an underlying L_X–M_{vir} correlation, as the growth rate of stellar mass is strongly coupled to the radiative cooling rate regulated by gravitational potential (e.g., J.-T. Li & Q. D. Wang 2013b). Consequently, gravitational heating and stellar feedback remain observationally degenerate based solely on scaling relations.

The launch of eROSITA in 2019 has enabled systematic measurements of X-ray emission in the circumgalactic medium (CGM) via stacking analysis of galaxy samples binned by properties such as the stellar mass (M_*) and specific SFR (sSFR; U. Chadayammuri et al. 2022; J. Comparat et al. 2022; Y. Zhang et al. 2024). For MW-mass galaxies, this approach has revealed extended X-ray emission out to the virial radius ($\gtrsim$100 kpc), with tentatively lower X-ray luminosities compared to both star-forming galaxies and more massive systems (e.g., J. Comparat et al. 2022; Y. Zhang et al. 2025).

A number of simulation studies have explored the properties of galactic coronal gas, e.g., X-ray luminosity, surface brightness, and scaling relations, using both cosmological hydrodynamical simulations (e.g., R. A. Crain et al. 2010; Á. Bogdán et al. 2015; A. J. Kelly et al. 2021; U. Chadayammuri et al. 2022; Y. Oren et al. 2024) and isolated high-resolution simulations (e.g., M. Li & S. Tonnesen 2020; R. Jana et al. 2024), primarily adopting external viewing perspectives. State-of-the-art simulations incorporating diverse physical processes can broadly reproduce certain observed coronal properties. However, large-scale simulations (e.g., IllustrisTNG and EAGLE) often exhibit an X-ray dichotomy at $z \sim 0$ driven by AGN feedback: at a transitional stellar mass of $M_* \sim 10^{10.5-11}\,M_\odot$, star-forming galaxies show elevated soft X-ray luminosities compared to quiescent systems (B. D. Oppenheimer et al. 2020; N. Truong et al. 2020). In contrast, isolated simulations enable precise modeling of SN-driven outflows but typically neglect AGN feedback and gas accretion from the IGM. These model-dependent limitations lead to divergent conclusions on fundamental issues, notably whether stellar feedback alone can explain hot corona origins (e.g., D. B. Henley et al. 2015; T. Peters et al. 2015).

Successful implementation of stellar feedback subgrid models in high-resolution zoom-in simulations offers critical insights into the origins of hot coronae in MW-type galaxies. The Stars and MUltiphase Gas in GaLaxiEs (SMUGGLE; F. Marinacci et al. 2019) is a physically motivated subgrid model for the ISM and stellar feedback that has reproduced key properties of stellar populations and cold ($T \lesssim 10^4$ K) interstellar gas (H. Li et al. 2020, 2022; A. Smith et al. 2022; E. D. Jahn et al. 2023; C. Li et al. 2024). Notably, our previous work (Z. Zhang et al. 2024) established that the SMUGGLE model accurately simulates Galactic warm ($T \sim 10^5$ K) gas traced by O VI absorption, capturing diagnostics such as scale heights and column density–line width relation. Here, we extend this validation to hot coronae ($T \sim 10^6$ K) in MW-mass systems, examining simulated X-ray properties from both external and solar (inside-out) perspectives. Given that the simulations model isolated disks with stellar feedback but exclude AGN activity and cosmological gas accretion, this work specifically tests whether stellar feedback alone can account for the observed X-ray signatures of halo gas. A comparison with observations allows us to assess whether additional heating mechanisms are necessary to generate extended, volume-filling hot coronae.

The paper is organized as follows. Section 2 describes the SMUGGLE model and the simulation suite analyzed in this work. Section 3 presents hot gas properties, including X-ray luminosity, surface brightness, emission measure, and temperature. These results are further discussed in Section 4, and in Section 5, we summarize our conclusions.

2. The SMUGGLE Model and Simulations

The high-resolution simulations we analyzed in this work were generated by a suite of runs performed with the SMUGGLE framework (F. Marinacci et al. 2019) as described in H. Li et al. (2020). SMUGGLE is a physically motivated subgrid model for the ISM and stellar feedback implemented within the moving-mesh code AREPO (V. Springel 2010). Below, we provide a brief overview of the model and simulation setup; detailed descriptions can be found in the original papers.

The SMUGGLE model incorporates various physical processes, including gravity, hydrodynamics, gas cooling and heating, star formation, and stellar feedback. Star particles are formed in cold, dense, and self-gravitating molecular gas reaching a density threshold of $n_{th} = 100\,\mathrm{cm}^{-3}$. The local SFR for star-forming gas cells is governed by the star formation efficiency (ϵ_{ff}) per freefall time, expressed as $\dot{M}_* = \epsilon_{ff} M_{gas}/\tau_{ff}$, where M_{gas} is the gas mass and τ_{ff} is the freefall time of the gas cell.

The model implements diverse channels of stellar feedback, categorized into two main types: (i) SN feedback, which injects substantial energy and momentum into the ISM; and (ii) early feedback, encompassing radiative processes (e.g., photoionization and radiation pressure) from massive stars, as well as stellar winds originating from both young OB stars and older asymptotic giant branch (AGB) stars. Feedback energy and momentum are deposited into the 64 nearest gas cells, weighted by the solid angle subtended by each cell relative to the star particle.

The high-resolution simulations model an isolated galactic disk. This disk consists of an MW-sized galaxy with a total mass of $1.6 \times 10^{12}\,M_\odot$. The galaxy's mass components include a stellar bulge ($1.5 \times 10^{10} M_\odot$), a stellar disk ($4.7 \times 10^{10} M_\odot$), a gaseous disk ($9 \times 10^9 M_\odot$), and a dark matter halo. The masses of these components are similar to those of the MW (see J. Bland-Hawthorn & O. Gerhard 2016, and references therein). The gaseous disk density decreases exponentially with a scale length of 6 kpc. The mass resolution of the simulations is about $1.4 \times 10^3\,M_\odot$ per gas cell, corresponding to the highest resolution runs in F. Marinacci et al. (2019). The gravitational softening for star particles is fixed at 7.2 pc, while for gas cells it is adaptively set with a minimum softening length of 3.6 pc. By varying the local star formation efficiency (ϵ_{ff}) and enabling/disabling different stellar feedback channels, six distinct subgrid models were simulated, as listed in Table 1.

In the following section, we present the properties of coronal gas in our simulated galaxies. We emphasize that no coronal component was included in the initial conditions; all coronal gas originates from internal galactic processes and is subsequently ejected. Throughout our analysis, we make no distinction between the ISM and CGM, defining hot halo gas as all gas cells at $T > 10^6$ K within the virial radius

Table 1
Summary of the Six Subgrid Model Variations Analyzed in This Work

Run	$\epsilon_{\rm ff}$	Radiation and Winds	SN
(1)	(2)	(3)	(4)
SFE1	0.01	✓	✓
SFE10	0.1	✓	✓
SFE100	1.0	✓	✓
Nofeed	0.01	✗	✗
Rad	0.01	✓	✗
SN	0.01	✗	✓

Note. Columns: (1) simulation run name; (2) star-formation efficiency; (3) inclusion of radiative feedback and stellar winds; (4) inclusion of SN feedback. SFE1 is the fiducial model with all stellar feedback channels enabled (F. Marinacci et al. 2019).

($R_{\rm vir} = 260$ kpc). This hot component constitutes a minor fraction ($\lesssim$10%) of the total gas mass within $R_{\rm vir}$.

3. Results

The diffuse X-ray emission depends on the gas density and temperature and is characterized by its emissivity. For hydrogen-dominated gas, the emissivity ϵ_ν (in units of erg s^{-1} cm^{-3} Hz^{-1}) is given by

$$\epsilon_\nu = n_e n_{\rm H} \Lambda_\nu(T,\ Z), \tag{1}$$

where ν is the frequency of emitted photons, n_e is the electron density, $n_{\rm H}$ is the hydrogen density, and Λ_ν is the cooling function for gas of temperature T and metallicity Z. The cooling function is dominated primarily by metal-line emission, with a secondary contribution from free–free emission (bremsstrahlung). The emissivity table is created using the Astrophysical Plasma Emission Code (APEC) model (R. K. Smith et al. 2001) within ATOMDB 3.0.9,[12] assuming an optically thin plasma in collisional ionization equilibrium. Assuming solar metallicity ($Z = Z_\odot$; e.g., D. B. Henley & R. L. Shelton 2013; S. Nakashima et al. 2018), the cooling function in the 0.5–2 keV band peaks between 10^6 and 10^7 K, and declines at both higher and lower temperatures.[13] The band-integrated emissivity is then given by

$$\epsilon_X = \int \epsilon_\nu d\nu. \tag{2}$$

Figure 1 shows face-on and edge-on projections of the 0.5–2 keV emissivity for the simulated galaxy in the final snapshot ($t = 0.775$ Gyr) of the SFE1 run, with zoom-ins on the central regions. As shown, the projected emissivity spans more than 10 orders of magnitude, with the highest values on average occurring in the central region. While diffuse features trace superbubbles driven by SNe, the embedded pointlike sources primarily arise from early feedback (stellar winds and/or radiation) from massive stars. In the edge-on view, the projected emissivity is low in the disk plane ($z \sim 0$) for $y \gtrsim 10$ kpc due to the scarcity of hot gas. This results from the declining stellar density at larger radii, which reduces feedback from massive stars and SNe, leaving the gaseous disk predominantly cold. Meanwhile, stellar feedback tends to channel energy and momentum more efficiently along the vertical direction than radially. The mushroom-shaped morphology indicates that SN feedback can extend to ~30 kpc above and below the galactic plane.

To compare with observations of X-ray emission from the MW and external disk galaxies, we derive the properties of hot gas surrounding our simulated galaxies using the `yt` analysis toolkit[14] (M. J. Turk et al. 2011). Unless otherwise stated, the X-ray properties discussed hereafter (e.g., luminosity and surface brightness) refer to the 0.5–2 keV band and analyses are performed using the final snapshot of the simulation run.

3.1. X-Ray Luminosity

The X-ray luminosity of a selected region is calculated as[15]

$$L_{\rm X} = \sum_i \epsilon_X \frac{m_i}{\rho_i}, \tag{3}$$

where ϵ_X, m_i, and ρ_i are the emissivity, mass, and density of the ith gas particle within the region, respectively. To enable a direct comparison with observations of external galaxies (J.-T. Li & Q. D. Wang 2013a), we calculate the luminosity within a cylindrical region centered on the galactic center. This cylinder extends vertically ±5 kpc from the disk midplane, corresponding to the median extent used for spectral analysis and luminosity calculation in the observed sample.

Figure 2(a) shows the evolution of X-ray luminosity within cylindrical regions of different radii for the fiducial SFE1 simulation. The luminosity integrated within the virial radius (260 kpc; black solid line) varies temporally and ultimately converges to the observed value for the MW ($L_{\rm X} = 2.0^{+3.0}_{-1.2} \times 10^{39}$ erg s^{-1}; S. L. Snowden et al. 1997; M. J. Miller & J. N. Bregman 2015) and for external disk galaxies with M_* and SFR comparable to the MW (gray band). The luminosity evolution generally traces the star formation history, exhibiting an initial sharp rise following the first episode of gravitational runaway collapse of molecular gas (see Figure 2 of H. Li et al. 2020). The luminosity within the central 1 kpc also evolves (blue dashed line) and typically contributes ~10%–50% of the total luminosity. The instances of the highest fractional contribution (nearly 50%) predominantly coincide with the sharp peak in the total luminosity. Since X-ray photons are primarily generated in the central region associated with stellar activity, the central concentration diminishes as activity subsides, allowing the emission to diffuse outward. Nevertheless, the diffuse X-ray emission remains concentrated within the central ~5 kpc (magenta dotted line). Notably, the total hot gas content is dominated by material beyond 5 kpc due to the large volume of these lower-density regions, i.e., hot gas at $5 < r < 260$ kpc constitutes about 99.5% of the total hot gas mass within the virial radius (260 kpc).

Figure 2(b) shows the evolution of X-ray luminosity within the cylindrical region extending to $r = 260$ kpc for the various simulation runs. All runs exhibit an initial sharp increase in X-ray luminosity, tracking the evolution of the SFR, triggered

[12] http://www.atomdb.org/

[13] Setting $Z = 0.3Z_\odot$ reduces 0.5–2 keV luminosity and surface brightness by approximately a factor of 3, and increases the emission measure by nearly the same factor.

[14] https://yt-project.org

[15] Luminosity is calculated using all gas particles within the selected region, including those in background grids. We confirmed that this background gas contributes only ~0.01%–3% of the time-averaged total luminosity, depending on the subgrid model.

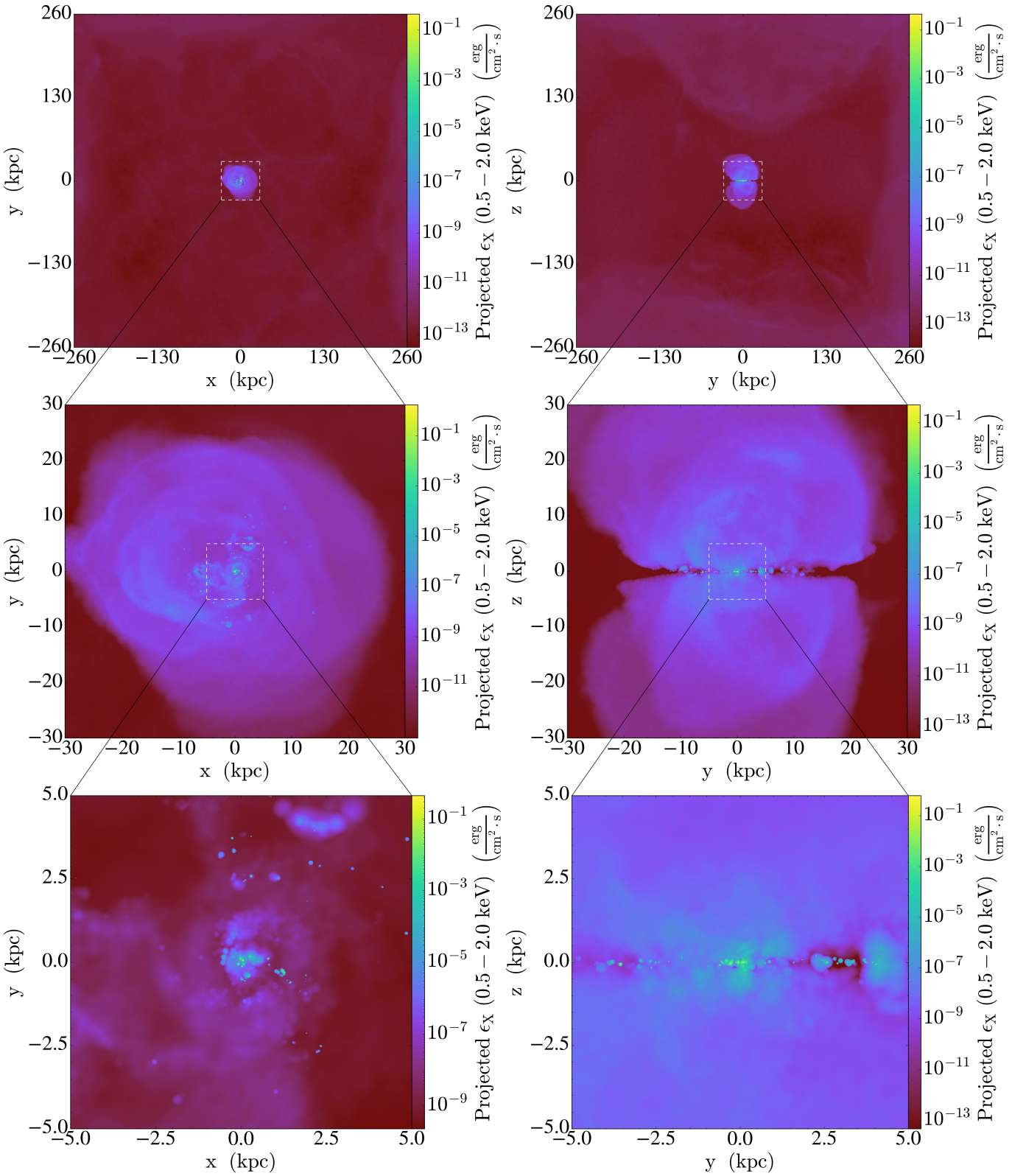

Figure 1. Projected 0.5–2 keV band emissivity along the z-axis (face-on; *left panels*) and the x-axis (edge-on; *right panels*) for the simulated galaxy in the SFE1 run at 0.775 Gyr. Rows show progressively zoom-in views (indicated by the white squares in the preceding row), with field-of-view side length of 520 kpc (top row), 60 kpc (middle row), and 10 kpc (bottom row), respectively.

by the first gravitational runaway collapse of molecular gas occurring after roughly one dynamical time. Subsequently, L_X oscillates with a declining trend. The *Nofeed* run exhibits significantly lower luminosities on average compared to the other runs, deviating from the observed range (gray band) by 1–2 orders of magnitude. The other runs show no significant differences among themselves. However, the SFE100 run, which has the highest star formation efficiency, displays

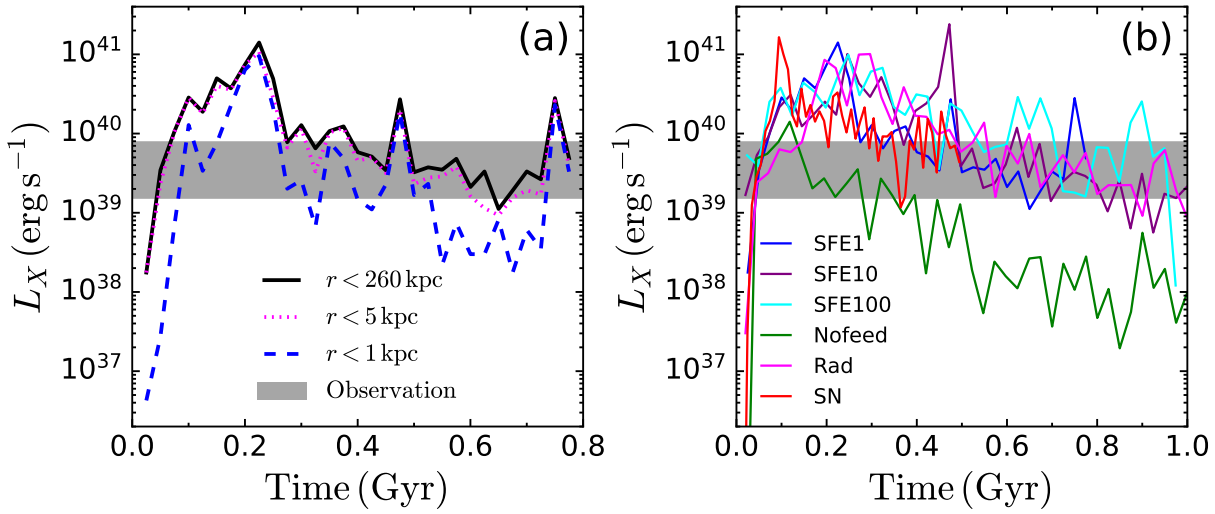

Figure 2. (a) Evolution of X-ray luminosity (L_X) within cylindrical regions (height = 10 kpc) of radii 260, 5, and 1 kpc for the simulated galaxy in the SFE1 run. The gray band indicates the observed L_X range for disk galaxies with stellar mass and SFR comparable to the MW (S. Mineo et al. 2012; Q. D. Wang et al. 2016); the MW itself resides within this band. (b) Time evolution of L_X within a cylindrical region (height = 10 kpc, radius = 260 kpc) for different simulation runs.

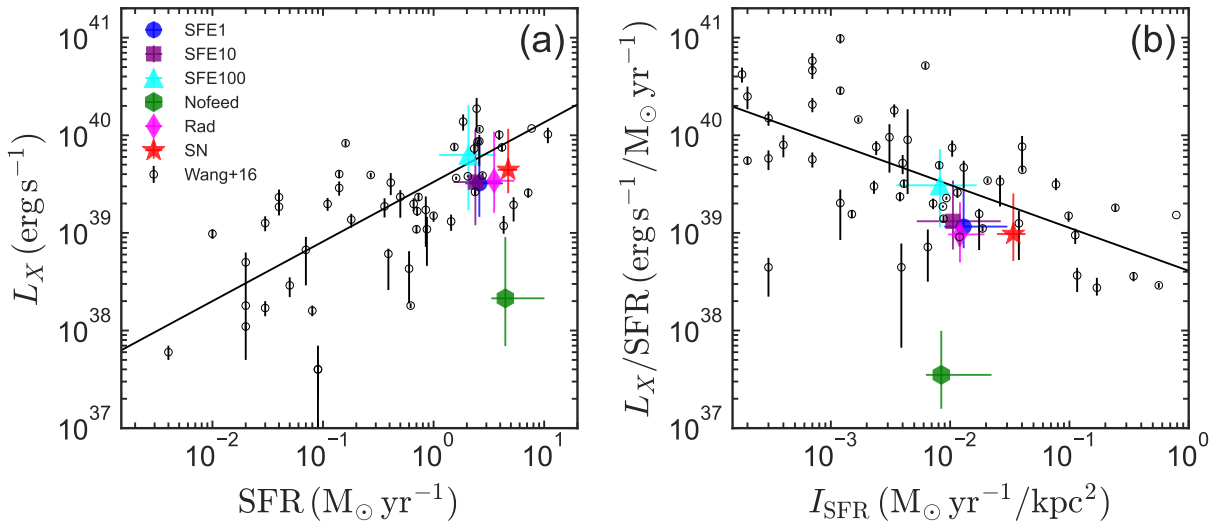

Figure 3. Comparison of model predictions (colored symbols) with observed scaling relations. (a) L_X–SFR relation for highly inclined disk galaxies in the local Universe (Q. D. Wang et al. 2016). Black circles show observational data; the solid line is the best-fit log-linear relation. Model L_X values were computed within cylinders of virial radius. The 1σ uncertainties (derived from the 16th and 84th percentiles) use snapshots at $t > 0.4$ Gyr. (b) L_X/SFR vs. I_{SFR} relation for the same galaxy sample.

violent oscillations, particularly at $\gtrsim$0.9 Gyr, crossing both above and below the observed range.

We also examine whether our simulated galaxies follow X-ray scaling relations similar to those observed in external disk galaxies. To calculate the medians and uncertainties of X-ray luminosity and SFR, we consider only snapshots at $t > 0.4$ Gyr and adopt a cylindrical radius of 260 kpc. The time cutoff ensures the gaseous disk has settled into a new equilibrium configuration and the multiphase ISM is fully developed. The SFR for each snapshot is averaged over 5 Myr.

Figure 3(a) displays the results from our simulation runs overplotted on the observed L_X–SFR relation for nearby highly inclined disk galaxies from Q. D. Wang et al. (2016). We find that the median SFR for all six runs falls within $\sim$2–5 $M_\odot$ yr^{-1}, consistent within uncertainties with observations of both the MW and external disk galaxies. While the *Nofeed* run underpredicts the diffuse X-ray luminosity by $\sim$1 dex, the X-ray luminosities predicted by the other runs generally agree with the observed relation (solid line), despite the large scatter of the relation. This agreement suggests that although early feedback mechanisms (stellar winds and radiation) from massive stars primarily heat gas on smaller spatial scales, they can ultimately produce X-ray luminosities comparable to those generated by SN feedback.

Figure 3(b) compares our simulation results with the observed L_X/SFR versus I_{SFR} relation for the same galaxy sample. Here $I_{SFR} \equiv SFR/(\pi R_{90}^2)$ represents the SFR surface density, where R_{90} is the radius enclosing 90% of the total SFR within a cylinder of height 20 kpc centered on the galaxy. Again, the *Nofeed* run is an outlier, exhibiting L_X/SFR values $\sim$1–2 orders of magnitude lower than observed. The other runs, however, show general agreement with the observed relation (Q. D. Wang et al. 2016). Our results suggest that while the subgrid model lacking feedback can be ruled out, the

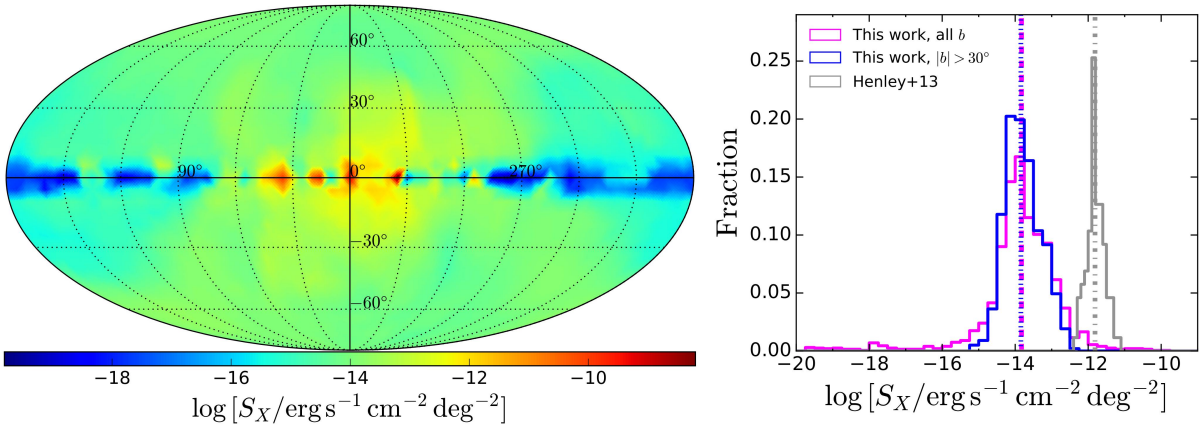

Figure 4. Left: all-sky X-ray surface brightness in Mollweide projection for an observer at the solar position. Right: comparison of the surface brightness distributions with XMM-Newton observations of the MW (gray histogram; 110 sightlines with $|b| > 30°$; D. B. Henley & R. L. Shelton 2013). The magenta and blue histograms show simulated results for all sightlines and $|b| > 30°$ sightlines, respectively. Lines of corresponding colors indicate the median values.

remaining subgrid models cannot be unambiguously distinguished based solely on these X-ray scaling relations.

3.2. X-Ray Surface Brightness

For an arbitrary line of sight, the surface brightness is obtained by integrating the emissivity along the path length s:

$$S_{\rm X} = \frac{1}{4\pi}\int \epsilon_X ds, \tag{4}$$

where the integration extends from 0 to 260 kpc, and $S_{\rm X}$ has units of erg s^{-1} cm^{-2} sr^{-1}. To compare with the MW observations, we place an observer at the Sun's location, which is 8.2 kpc from the galactic center in the disk plane (J. Bland-Hawthorn & O. Gerhard 2016). Specifically, the observer's coordinates are $(x_0 + 8.2, y_0, z_0)$, where (x_0, y_0, z_0) denote the galactic center coordinates in units of kiloparsecs. The lines of sight are defined by their Galactic coordinates (l, b).

The resulting all-sky map of the surface brightness is shown in the left panel of Figure 4. This map was generated by first dividing the entire sky into a grid with $\Delta l = 5°$ and $\Delta b = 5°$, calculating $S_{\rm X}$ for each grid line of sight, and then linearly interpolating to obtain values on a finer grid with $0.^{\circ}5$ resolution. As shown, $S_{\rm X}$ varies significantly across different lines of sight, differing by $\gtrsim$10 orders of magnitude, consistent with the emissivity distribution shown in Figure 1. The highest and lowest surface brightness both occur near the disk plane: toward the galactic center ($l \sim 0°$) and anticenter ($l \sim 180°$) directions, respectively. This behavior directly reflects the projected emissivity results in Figure 1. The X-ray emission originates predominantly from the central few kiloparsecs due to the higher density of hot gas. Consequently, for an observer at the Sun's location, only sightlines passing through these central regions exhibit high surface brightness.

To mitigate potential biases arising from using a single observer at a specific location, we place four observers at off-center positions. Each observer is located 8.2 kpc from the galactic center, with their positions separated by 90° azimuthally (e.g., Y. Zheng et al. 2020; Z. Zhang et al. 2024). For each observer, we generate 500 random lines of sight and calculate the corresponding surface brightness. The Galactic longitude l is generated uniformly over [0°, 360°), while the latitude b is generated over [−90°, 90°] with a probability density proportional to cos(b), i.e., $P(b) \propto \cos(b)$.

The right panel of Figure 4 displays the distribution of surface brightness for a total of 2000 sightlines (500 per observer × 4 observers). Unlike the narrow distribution (∼1 dex) observed for the Galactic halo (gray histogram; D. B. Henley & R. L. Shelton 2013), the simulated galaxy's surface brightness exhibits a strong dependence on the sightline orientation (magenta histogram). Sightlines penetrating the central region (e.g., $|b| \lesssim 10°$ and $|l| \lesssim 30°$[16]) show brightness comparable to or even exceeding the observed ranges. In contrast, antigalactic sightlines can exhibit surface brightness 4–8 orders of magnitude lower than the observed values. When applying observational constraints such as $|b| > 30°$ (blue histogram), both the brightest and darkest sightlines are excluded. This results in a median value nearly identical to the unconstrained case; however, our median results under these constraints remain ∼2 orders of magnitude lower than the observations.

To compare with the stacking results for approximately 80,000 MW-mass galaxies from eROSITA (Y. Zhang et al. 2024), we present the surface brightness profile from external views in Figure 5(a). This profile was generated similarly to the observational methodology but incorporates various galaxy orientations. In our simulations, the surface brightness generally declines with increasing radius. The profile steepens beyond $r \gtrsim 5$ kpc compared to the inner region. This results in an underestimation of the surface brightness in the outer regions ($r \gtrsim 10$ kpc) by at least 2 orders of magnitude, consistent with the inside-out view result shown in Figure 4(b). As observational data for the inner regions are unavailable, a direct comparison in this radial range is not possible.

Figure 5(b) compares the surface brightness for various subgrid models, from a solar perspective (similar to Figure 4). Simulations including SN feedback align more closely with observational determinations, largely owing to the large-scale superbubbles driven by SN explosions. However, even for the best-matching SN run, a discrepancy of ∼1.5 dex remains when comparing median values.

[16] In our notation, this longitude interval corresponds to $l \lesssim 30°$ or $l \gtrsim 330°$.

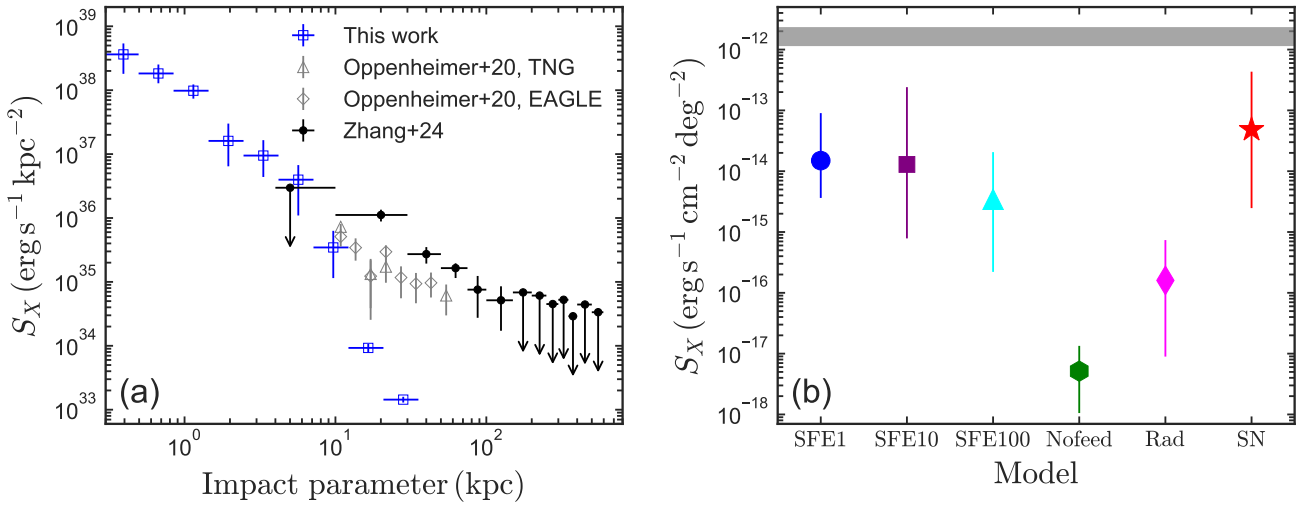

Figure 5. (a) Surface brightness profile for the SFE1 run compared to eROSITA observations of MW-mass stacks (black circles; Y. Zhang et al. 2024). Results from EAGLE (gray diamonds) and IllustrisTNG (gray triangles) for low-mass, low-sSFR galaxies are overplotted (see B. D. Oppenheimer et al. 2020 for sample selection criteria). (b) Median surface brightness with 1σ uncertainties for different subgrid models (solar perspective). The gray band shows the observed range for the Galactic halo (D. B. Henley & R. L. Shelton 2013).

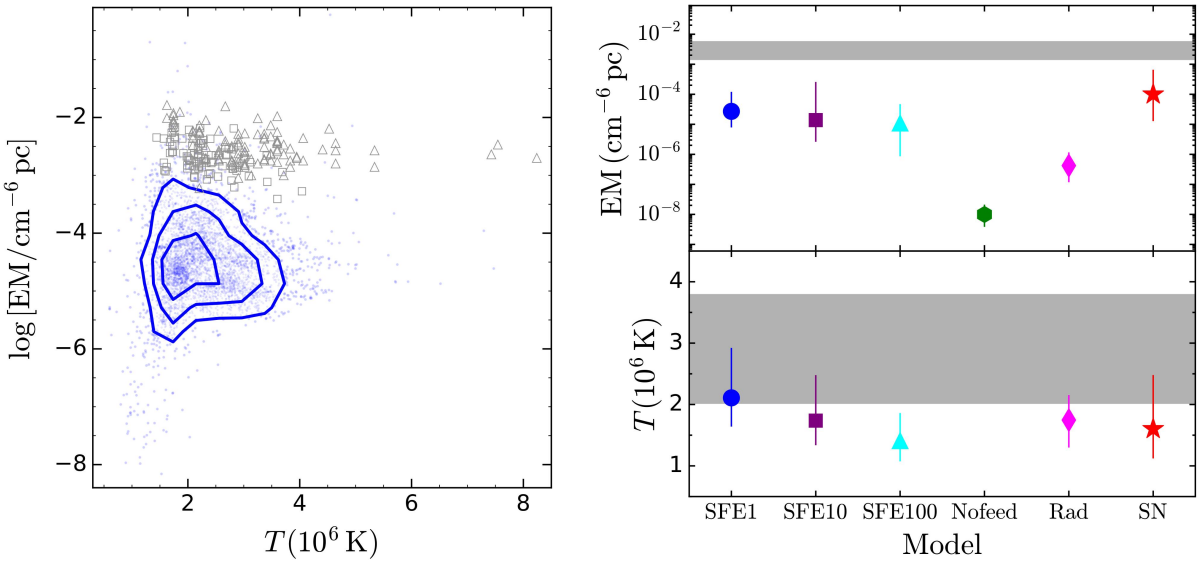

Figure 6. Left: emission measure vs. emissivity-weighted temperature. Blue dots show results from the SFE1 run; blue contours indicate the 1σ–3σ confidence levels. Gray symbols represent observations: squares from XMM-Newton (D. B. Henley & R. L. Shelton 2013) and triangles from Suzaku (S. Nakashima et al. 2018). Right: predicted emission measure and temperature for different simulation runs. The gray band marks the observed 1σ range from combined XMM-Newton and Suzaku data.

3.3. Emission Measure and Temperature

The emission measure (EM), along with the temperature (T), determines the emissivity. EM and T can be simultaneously derived by fitting X-ray spectra with plasma models (e.g., APEC), often under the simplifying assumption of a single-temperature ($1T$) component, despite significant temperature variations potentially existing along the sightline.

The emission measure is calculated as

$$\mathrm{EM} = \int n_e n_{\mathrm{H}} ds, \tag{5}$$

where the integration extends from 0 to 260 kpc.

To make a relatively straightforward comparison with observations, we adopt the emissivity-weighted temperature along the sightline as the "measured" temperature (e.g., F. Guo et al. 2020). Given that $1T$ models typically yield $T \gtrsim 10^6$ K for the Galactic hot halo, we calculated EM by considering only gas particles with $T > 10^6$ K (e.g., D. B. Henley et al. 2015).

Figure 6(a) displays the EM$-T$ distribution for 5000 random sightlines originating from four off-center observers in the SFE1 run. The predicted temperature distribution (blue dots and contours) is broadly consistent with observations (gray squares and triangles; D. B. Henley & R. L. Shelton 2013; S. Nakashima et al. 2018), with median temperatures of $2.1^{+0.8}_{-0.5} \times 10^6$ K and $3.0^{+0.8}_{-0.1} \times 10^6$ K, respectively. However, the EM values are systematically underestimated by $\sim$2 orders of magnitude. The discrepancy arises because denser hot gas particles are predominantly concentrated within the central $\sim$5 kpc, causing most random sightlines from off-center observers to avoid this high-density region.

The EM$-T$ distributions for other simulation runs are similarly derived and compared in Figure 6(b). The dependence

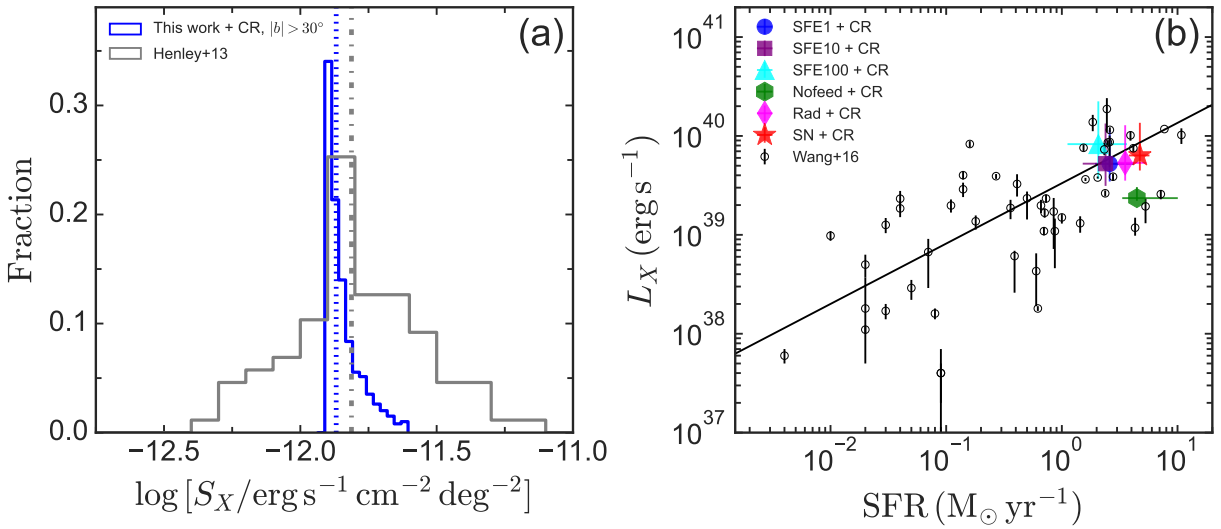

Figure 7. (a) Surface brightness distribution (methodology identical to Figure 4(b)), including contributions from inverse Compton scattering of CMB photons by cosmic rays (blue). (b) L_X–SFR relation (see Figure 3) incorporating cosmic-ray effects.

of EM on subgrid models follows a trend analogous to that of surface brightness in Figure 5(b), as expected since both quantities scale with the square of gas density. Furthermore, all simulated EMs fall below observational constraints (gray band; D. B. Henley & R. L. Shelton 2013; S. Nakashima et al. 2018). Temperatures from most models (SFE1, SFE10, Rad, and SN) remain consistent with observations within uncertainties. The *Nofeed* run is excluded due to insufficient hot gas production, rendering its inferred temperature physically unmeaningful.

4. Discussion

4.1. Comparison with the Literature

In Section 3, we analyzed high-resolution simulations of isolated galaxies from both internal (inside-out) and external perspectives. The results demonstrate that the SMUGGLE model broadly reproduces the X-ray luminosity of MW-mass disk galaxies across various stellar-feedback subgrid models. However, X-ray emission predominantly originates from the central ∼5 kpc region. This spatial concentration leads to underestimations of surface brightness and emission measure by ∼2 orders of magnitude for inside-out sightlines.

Similar discrepancies were reported by D. B. Henley et al. (2015), whose magnetohydrodynamical model of SN-driven ISM (A. S. Hill et al. 2012) yielded comparable results. They proposed that key physical processes such as charge exchange emission, cosmic-ray-driven outflows, and accretion-powered extended gaseous halos may be essential for reconciling simulations with observations.

Additional studies have compared cosmological simulations with X-ray observations of MW-mass systems. These typically employ mock X-ray observations of individual galaxies or galaxy stacks from external views (e.g., N. Truong et al. 2020; A. J. Kelly et al. 2021). For instance, B. D. Oppenheimer et al. (2020) detected diffuse X-ray emission in the CGM of low-sSFR MW-mass galaxies within the EAGLE (J. Schaye et al. 2015) and IllustrisTNG (A. Pillepich et al. 2018) simulations. The derived X-ray luminosity within 10–200 kpc reaches $L_X \sim 10^{39}\,\mathrm{erg\,s^{-1}}$, approximately half the value measured for the MW (S. L. Snowden et al. 1997). Furthermore, both simulations underpredict the eROSITA stacked surface brightness of MW-mass galaxies (Y. Zhang et al. 2024) by factors of ∼5–10 (gray diamonds and triangles in Figure 5(a)).

N. Truong et al. (2020) conducted mock X-ray observations of galaxies across a broad mass range in the IllustrisTNG simulations. They found that the 0.3–5 keV luminosity within R_e and $5R_e$ for MW-mass galaxies is consistent with Chandra observations of late-type galaxies (S. Mineo et al. 2012; J.-T. Li & Q. D. Wang 2013a). Additionally, they confirmed the dependence of X-ray luminosity on SFR in low-mass galaxies and reported a systematic difference between star-forming and quenched systems: the former exhibits X-ray luminosities approximately 1 order of magnitude higher on average. They attributed this disparity to galaxy quenching driven by kinetic AGN feedback from supermassive black holes—a process absent in our current simulations.

A. J. Kelly et al. (2021) investigated the origin of X-ray coronae in central disk galaxies using the EAGLE simulations (J. Schaye et al. 2015). Their results show good agreement between simulated X-ray luminosities of MW-mass galaxies and observational data. Furthermore, they demonstrated that while SN-heated gas dominates the X-ray emission within the central region ($\leqslant 0.1R_{\mathrm{vir}}$), a quasi-hydrostatic, accreted atmosphere prevails beyond this radius for galaxies of mass $\leqslant 10^{12}\,M_\odot$.

Including a galactic hot corona may resolve the tension between our results and observations. The hot corona plays a fundamental role in galaxy evolution. When implemented in initial conditions analogous to our simulations (e.g., F. Barbani et al. 2023, 2025), such coronae establish a gas reservoir essential for sustaining star formation. This process drives a gas circulation cycle (the galactic fountain) between the disk and corona, mediated by stellar feedback. We reserve analysis of corona-embedded simulations for future investigation.

4.2. The Impact of Cosmic Rays

While gas heating via cosmic-ray interactions is implemented in the SMUGGLE model, this effect primarily applies to dense gas. Recently, P. F. Hopkins et al. (2025) proposed that inverse Compton scattering of cosmic microwave background (CMB) photons by GeV cosmic-ray electrons could be responsible for the diffuse X-ray emission in low-mass systems. Here, we

examine whether incorporating this effect can improve the agreement of the SMUGGLE model with observations.

Figure 7(a) shows surface brightness distribution for the SFE1 run, now including cosmic-ray-induced hot gas via the inverse Compton process (blue histogram). We adopt a leptonic energy injection rate of $\dot{E}_{40} \equiv \dot{E}_{\rm cr,l}/10^{40}\,{\rm erg\,s^{-1}} = 0.2$ and a streaming speed of $v_{100} \equiv v_{\rm st,eff}/100\,{\rm km\,s^{-1}} = 1.0$ (see Equation (6) of P. F. Hopkins et al. 2025). The results from their Figures 2 and 4 are then rescaled to update the surface brightness and luminosity according to these parameters. While the median surface brightness now shows good agreement with observations (vertical lines), our results exhibit a narrower distribution dominated by cosmic-ray effects.

Figure 7(b) presents the $L_{\rm X}$–SFR relation, now incorporating cosmic-ray effects. The results remain consistent with Chandra observations of nearby disk galaxies and, in fact, show improved agreement compared to those presented in Figure 3(a).

However, the agreement of both the surface brightness distribution and the total luminosity with observations does not necessarily imply that cosmic rays are the sole or correct solution. Instead, this demonstrates that any mechanism capable of contributing to the development of a hot CGM, such as AGN feedback and/or gas accretion from the IGM, may help reconcile the model with the observations. Crucially, while the surface brightness increases by ∼2 dex in this scenario, the total X-ray luminosity remains consistent with the observed values.

5. Summary

We study diffuse X-ray emission from hot gaseous halos in MW-like galaxies by analyzing a series of high-resolution simulations using the SMUGGLE galaxy formation model. Our analysis incorporates both inside-out (solar location) and external perspectives. The main conclusions are as follows.

1. For the five subgrid models with stellar feedback included, the overall X-ray luminosities agree with MW observations and scaling relations for external disk galaxies. This suggests that early feedback (stellar wind and radiation) from massive stars contributes X-ray luminosities comparable to those from SN explosions, despite its more localized impact.
2. Viewed from the solar location, all simulations underpredict the median surface brightness of the MW by ∼1–5 orders of magnitude. This occurs because the simulated denser hot gas is concentrated within the central ∼5 kpc, leaving most random sightlines devoid of luminous X-ray-emitting regions. This radial concentration is confirmed by the external view: the simulated surface brightness profile underestimates observations of MW-mass galaxy stacks beyond ∼10 kpc by $\gtrsim$2 orders of magnitude.
3. The emissivity-weighted temperatures across simulations generally match MW observations. However, all runs underestimate the EM by ∼1–5 orders of magnitude.
4. Including inverse Compton scattering of CMB photons by cosmic rays alleviates the tension: the median surface brightness becomes consistent with MW observations while maintaining consistency with observed luminosity. Incorporating a hot coronal component in the initial conditions may also help. Alternatively, solutions could involve AGN feedback and/or gas accretion from the IGM.

The SMUGGLE model successfully reproduces the kinematics and spatial distributions of warm gas traced by O VI absorption (Y. Faerman et al. 2017, 2020; Z. Zhang et al. 2024). The inconsistency between the simulated X-ray coronae and observations indicates that the origins of hot gas (at least partially) differ from those of cooler gas. Studying absorptions of highly ionized metal species (e.g., O VII and O VIII) would help elucidate the detailed effects of different stellar feedback channels on hot gas. Future versions of the SMUGGLE model will incorporate cosmological simulations and serve as a powerful tool for predicting multiphase gas properties.

Acknowledgments

X.Z. thanks Zhijie Qu for helpful discussions on various aspects of this work. This work is supported by the National Natural Science Foundation of China (grant Nos. 11890692, 12133008, 12221003, 12273031, 12192220, 12192223, and 12361161601), the China Manned Space Program (grant NoS. CMS-CSST-2025-A10 and CMS-CSST-2021-B02), the Fundamental Research Fund for the Central Universities of China (grant No. 20720230016), the Fujian Provincial Natural Science Foundation of China (grant No. 2024J08001), and the Natural Science Foundation of Xiamen, China (No. 3502Z202472007). F.M. acknowledges funding by the European Union—NextGenerationEU, in the framework of the HPC project—"National Centre for HPC, Big Data and Quantum Computing" (PNRR—M4C2—I1.4—CN00000013—CUP J33C22001170001). Q.Y. was supported by the European Research Council (ERC) under grant agreement No. 101040751.

Software: yt (M. J. Turk et al. 2011), Astropy (Astropy Collaboration et al. 2018), Matplotlib (J. D. Hunter 2007), SciPy (P. Virtanen et al. 2020).

ORCID iDs

Zhijie Zhang (张志杰) https://orcid.org/0000-0002-8552-2558
Xiaoxia Zhang (张小霞) https://orcid.org/0000-0003-4832-9422
Hui Li (李辉) https://orcid.org/0000-0002-1253-2763
Taotao Fang (方陶陶) https://orcid.org/0000-0002-2853-3808
Yang Luo (罗阳) https://orcid.org/0000-0002-2243-2790
Federico Marinacci https://orcid.org/0000-0003-3816-7028
Laura V. Sales https://orcid.org/0000-0002-3790-720X
Paul Torrey https://orcid.org/0000-0002-5653-0786
Mark Vogelsberger https://orcid.org/0000-0001-8593-7692
Qingzheng Yu (余清正) https://orcid.org/0000-0003-3230-3981
Feng Yuan (袁峰) https://orcid.org/0000-0003-3564-6437

References

Astropy Collaboration, Price-Whelan, A. M., Sipőcz, B. M., et al. 2018, AJ, 156, 123
Barbani, F., Pascale, R., Marinacci, F., et al. 2023, MNRAS, 524, 4091
Barbani, F., Pascale, R., Marinacci, F., et al. 2025, A&A, 697, A121
Bland-Hawthorn, J., & Gerhard, O. 2016, ARA&A, 54, 529
Bogdán, Á., Vogelsberger, M., Kraft, R. P., et al. 2015, ApJ, 804, 72
Chadayammuri, U., Bogdán, Á., Oppenheimer, B. D., et al. 2022, ApJL, 936, L15
Comparat, J., Truong, N., Merloni, A., et al. 2022, A&A, 666, A156
Crain, R. A., McCarthy, I. G., Frenk, C. S., Theuns, T., & Schaye, J. 2010, MNRAS, 407, 1403

Davé, R., Finlator, K., & Oppenheimer, B. D. 2012, MNRAS, 421, 98
Faerman, Y., Sternberg, A., & McKee, C. F. 2017, ApJ, 835, 52
Faerman, Y., Sternberg, A., & McKee, C. F. 2020, ApJ, 893, 82
Fang, T., Buote, D., Bullock, J., & Ma, R. 2015, ApJS, 217, 21
Fang, T., Mckee, C. F., Canizares, C. R., & Wolfire, M. 2006, ApJ, 644, 174
Fang, T., Sembach, K. R., & Canizares, C. R. 2003, ApJL, 586, L49
Guo, F., Zhang, R., & Fang, X.-E. 2020, ApJL, 904, L14
Henley, D. B., & Shelton, R. L. 2013, ApJ, 773, 92
Henley, D. B., Shelton, R. L., Kwak, K., Hill, A. S., & Mac Low, M.-M. 2015, ApJ, 800, 102
Hill, A. S., Joung, M. R., Mac Low, M.-M., et al. 2012, ApJ, 750, 104
Hopkins, P. F., Quataert, E., Ponnada, S. B., & Silich, E. 2025, OJAp, 8, 78
Hunter, J. D. 2007, CSE, 9, 90
Jahn, E. D., Sales, L. V., Marinacci, F., et al. 2023, MNRAS, 520, 461
Jana, R., Sarkar, K. C., Stern, J., & Sternberg, A. 2024, MNRAS, 531, 2757
Kelly, A. J., Jenkins, A., & Frenk, C. S. 2021, MNRAS, 502, 2934
Li, C., Li, H., Cui, W., et al. 2024, MNRAS, 529, 4073
Li, H., Vogelsberger, M., Bryan, G. L., et al. 2022, MNRAS, 514, 265
Li, H., Vogelsberger, M., Marinacci, F., Sales, L. V., & Torrey, P. 2020, MNRAS, 499, 5862
Li, J.-T., & Wang, Q. D. 2013a, MNRAS, 428, 2085
Li, J.-T., & Wang, Q. D. 2013b, MNRAS, 435, 3071
Li, M., & Tonnesen, S. 2020, ApJ, 898, 148
Luo, Y., Fang, T., & Ma, R. 2018, ApJS, 235, 28
Marinacci, F., Sales, L. V., Vogelsberger, M., Torrey, P., & Springel, V. 2019, MNRAS, 489, 4233
Miller, M. J., & Bregman, J. N. 2015, ApJ, 800, 14
Mineo, S., Gilfanov, M., & Sunyaev, R. 2012, MNRAS, 426, 1870
Nakashima, S., Inoue, Y., Yamasaki, N., et al. 2018, ApJ, 862, 34
Oppenheimer, B. D., Bogdán, Á., Crain, R. A., et al. 2020, ApJL, 893, L24
Oren, Y., Sternberg, A., McKee, C. F., Faerman, Y., & Genel, S. 2024, ApJ, 974, 291
Pan, Z., Qu, Z., Bregman, J. N., & Liu, J. 2024, ApJS, 271, 62
Peters, T., Girichidis, P., Gatto, A., et al. 2015, ApJL, 813, L27
Pillepich, A., Springel, V., Nelson, D., et al. 2018, MNRAS, 473, 4077
Schaye, J., Crain, R. A., Bower, R. G., et al. 2015, MNRAS, 446, 521
Smith, A., Kannan, R., Tacchella, S., et al. 2022, MNRAS, 517, 1
Smith, R. K., Brickhouse, N. S., Liedahl, D. A., & Raymond, J. C. 2001, ApJL, 556, L91
Snowden, S. L., Egger, R., Freyberg, M. J., et al. 1997, ApJ, 485, 125
Sokołowska, A., Babul, A., Mayer, L., Shen, S., & Madau, P. 2018, ApJ, 867, 73
Spitzer, L., Jr 1956, ApJ, 124, 20
Springel, V. 2010, MNRAS, 401, 791
Strickland, D. K., Heckman, T. M., Colbert, E. J. M., Hoopes, C. G., & Weaver, K. A. 2004, ApJ, 606, 829
Truong, N., Pillepich, A., Werner, N., et al. 2020, MNRAS, 494, 549
Tüllmann, R., Pietsch, W., Rossa, J., Breitschwerdt, D., & Dettmar, R. J. 2006, A&A, 448, 43
Turk, M. J., Smith, B. D., Oishi, J. S., et al. 2011, ApJS, 192, 9
Virtanen, P., Gommers, R., Oliphant, T. E., et al. 2020, NatMe, 17, 261
Wang, Q. D., Li, J., Jiang, X., & Fang, T. 2016, MNRAS, 457, 1385
White, S. D. M., & Frenk, C. S. 1991, ApJ, 379, 52
White, S. D. M., & Rees, M. J. 1978, MNRAS, 183, 341
Zhang, Y., Comparat, J., Ponti, G., et al. 2024, A&A, 690, A267
Zhang, Y., Comparat, J., Ponti, G., et al. 2025, A&A, 693, A197
Zhang, Z., Zhang, X., Li, H., et al. 2024, ApJ, 962, 15
Zheng, Y., Peeples, M. S., O'Shea, B. W., et al. 2020, ApJ, 896, 143